Fast Kinetics Design for Solid-State Battery Device

*Yichao Wang and Xin Li**

Fast kinetics of solid-state batteries at the device level is not adequately explored to achieve fast charging and discharging. In this work, a leap forward is achieved for fast kinetics in full cells with high cathode loading and areal capacity. This kinetic improvement is achieved by designing a hierarchical structure of electrode composites. In the cathode, the authors' design enables high areal capacities above 3 mAh cm^{-2} to be stably cycled at high current densities of ≈13–40 mA cm^{-2}, yielding a C-rate from 5 to 10 C. In the anode, the authors' design breaks the common rule of the negative correlation between critical C-rate and the discharge voltage that is observed in most other anodes. The overall design enables the fast cycling of such batteries for over 4000 cycles at room temperature and 5 C charge-rate. The design principles unveiled by this work help to understand critical kinetic processes in battery devices that limit the fast cycling at high cathode loading and speed up the design of high-performance solid-state batteries.

1. Introduction

Solid-state batteries (SSBs) are considered a promising next generation battery technology with high energy density and safety for electric vehicles. Sulfide solid electrolytes, in comparison with other electrolyte types, are attractive due to the high ionic conductivity.[1] Although the material-level ionic conductivity can always help the device-level ionic transport, it often is not sufficient for enabling high power density. Such power density is frequently limited by factors such as lithium dendrite growth and electrode tortuosity. In addition, power density and energy density usually exhibit a trade-off relationship. A cyclable battery nowadays can show high C-rate (> ≈4–40 C) at low cathode loading (≈2 mg cm^{-2}),[2–7] but at commercial-relevant cathode loading (e.g., >15 mg cm^{-2}), the C-rate has to be significantly reduced to < 1.5 C at room temperature (RT) and < 2.5 C at ≈60 °C (**Figure 1**).[6,8,9]

Although the drop of ionic conductivity for solid electrolyte materials with decreasing temperature is an order of magnitude less severe than with liquid electrolytes, the device level capacity often still drops fast in SSB at lower temperatures. This reflects slow kinetics at the device level rather than at the material level.

Thus, a high areal capacity (>1 mAh cm^{-2}) with less than 15 min charge (and discharge) time (>4 C-rate) has been challenging, no matter at RT or even above 50 °C (Figure 1). All these facts suggest that fast kinetics of SSBs at the device level has not been adequately explored.

SSB technology in fact provides unique opportunities to design new structures for battery devices. For cathodes, mixing large particle size of cathode materials with small particle size of solid electrolyte materials[10,11] has been used to increase ionic percolation in the thick cathode layer to obtain high capacity at low C-rate.[10] Similarly, low tortuosity Li ion conduction network of oxide solid electrolyte has been achieved through 3D printing or freeze casting techniques.[12,13] In the separator layer, multi-electrolyte-layer configuration has been used to prevent Li dendrite penetration.[2–4] For anodes, Si or Ag can achieve a long cycle life at elevated temperature and low C-rate.[8,9,14] However, such a device design for extremely fast kinetics at high areal capacity has not been reported.

In this work, we design fast device kinetics through hierarchical composite structures for Li-ion SSBs with high loading and areal capacity. We demonstrate both high power and high energy densities at RT and in a broad temperature range as well (Figure 1a). The battery design is ≈5–7 times faster at areal capacities of ≈3–4 mAh cm^{-2}. In addition, this device design broadens the fast kinetics capability to achieve higher areal capacities of 10 mAh cm^{-2}, in comparison with previous reports at comparable separator layer thickness and stack pressure of pressurized coin cells. Note that we neglect reports at very low areal capacities in the comparison. Our battery configuration is illustrated in Figure 1b, with the schemes to illustrate the mechanism in Figure 1c,d. For cathode composite (Figure 1c), we demonstrate, for the first time, that the electrolyte mixture with designed ratio between small (≈300 nm to 4 um) and large (≈20 um) particles (right panel) provides the best high rate performance. This design benefits from the intimate interface contact between cathode and electrolyte particles from nano to submicron scale and from the fast Li transport with low tortuosity through the large micron sized electrolyte particles in the catholyte matrix as well. In contrast, cases of large catholyte only (left panel) and small catholyte only (middle panel) will either lack sufficient interface contact or suffer from large tortuosity, respectively. For anode composite (Figure 1d), we mix solid electrolyte with silicon particles in one layer and make graphite as a separation layer to the Li metal layer in the battery assembly. This design first increases the C-rate

Y. Wang, X. Li
John A. Paulson School of Engineering and Applied Sciences
Harvard University
Cambridge, MA 02138, USA
E-mail: lixin@seas.harvard.edu

**ADVANCED
SCIENCE NEWS**

www.advancedsciencenews.com
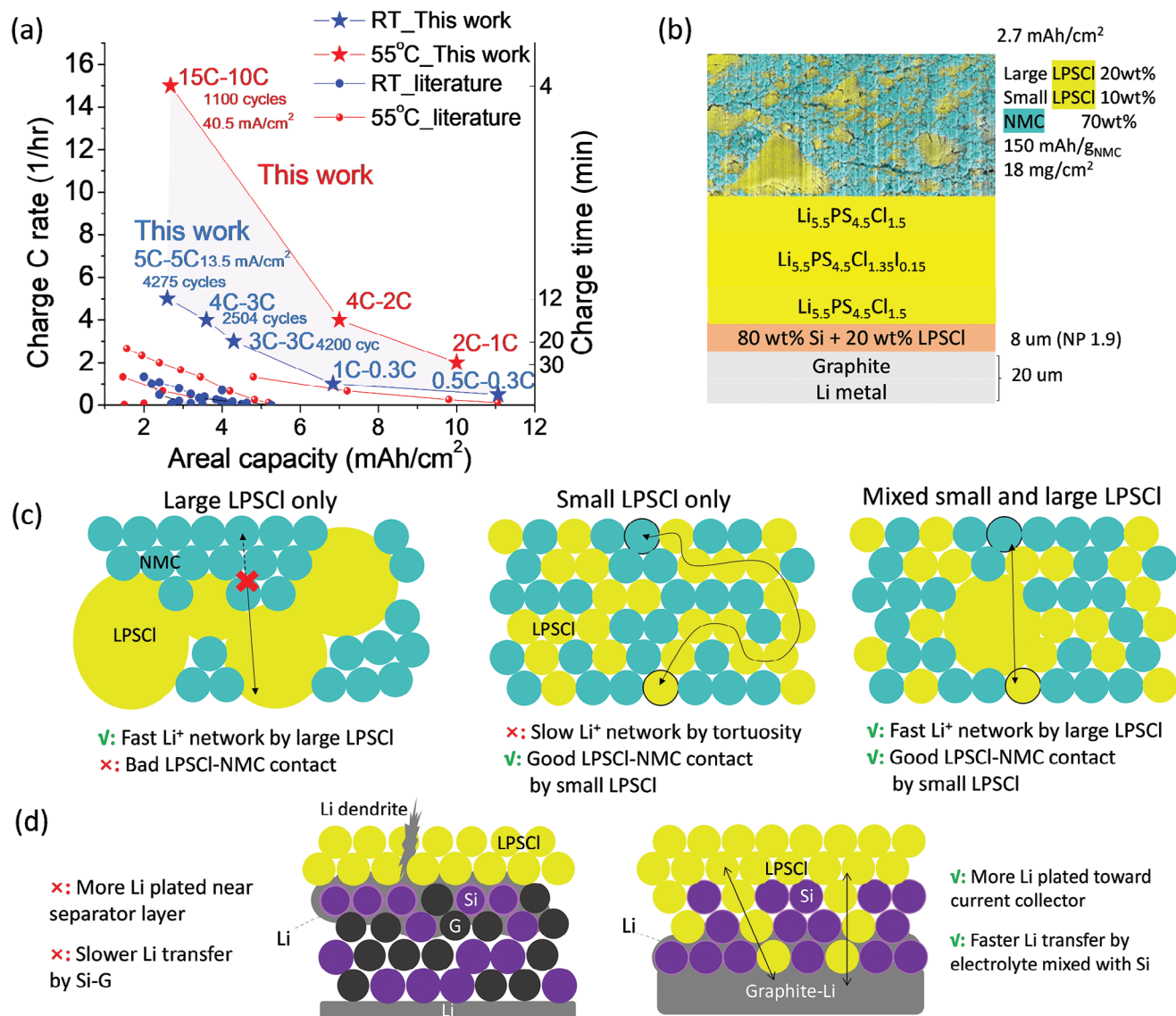
**ADVANCED
MATERIALS**

www.advmat.de

Figure 1. a) Critical C-rate at different areal capacity of our solid-state batteries at RT and 55 °C in this work (stars), in comparison with literature (dots).[6,8,9,15–19] Reproduced with permission. [6] Copyright 2023, Springer Nature. [8] Copyright 2021, AAAS. [9] Copyright 2022, Wiley. [15] Copyright 2021, Wiley. [16] Copyright 2020, Wiley. [17] Copyright 2021, Springer Nature. [18] Copyright 2021, ACS. [19] Copyright 2018, ACS. b) Illustration of battery configuration of a 2.7 mAh cm^{-2} battery. c) Illustration of the mechanism of fast Li ion transport kinetics from catholyte network with mixed particle sizes (right panel) in comparison with large (left panel) and small (middle panel) catholyte-only cases. d) Illustration of the effect of sulfide anolyte mixed with Si to better transport Li toward the current collector to prevent Li dendrite penetration (right panel), in comparison with no electrolyte mixed in the Si-graphite (G) layer (left panel). Note that this illustrates the effect at an extremely fast C-rate; while, at medium or low C-rate, both anode designs can work well.

capability as more Li metal is transported by the electrolyte mixed in the Si layer to plate toward the current collector (right panel), which better inhibits the Li dendrite growth than a pure Si or Si-graphite layer without mixing with solid electrolyte particles, where Li tends to plate near the separator layer due to the diffusion limit of Si or graphite (left panel). In addition, our design also causes less lithiation of Si due to the transport of Li through the solid electrolyte in the Si layer and more Li plating toward the current collector, giving a lower anode voltage, and hence, higher cell voltage. Our work provides new design principles of fast device kinetics in SSBs for high power densities with long

cycling stability, which will be important to the applications of high-performance battery devices when power density becomes crucial.

2. Results and Discussion

2.1. Electrochemical Performance With Fast Kinetics Design

We first demonstrate that cell configuration design for cathode and anode layers can dramatically increase the rate performance of full cells at RT (**Figure 2a**). First, we use the two
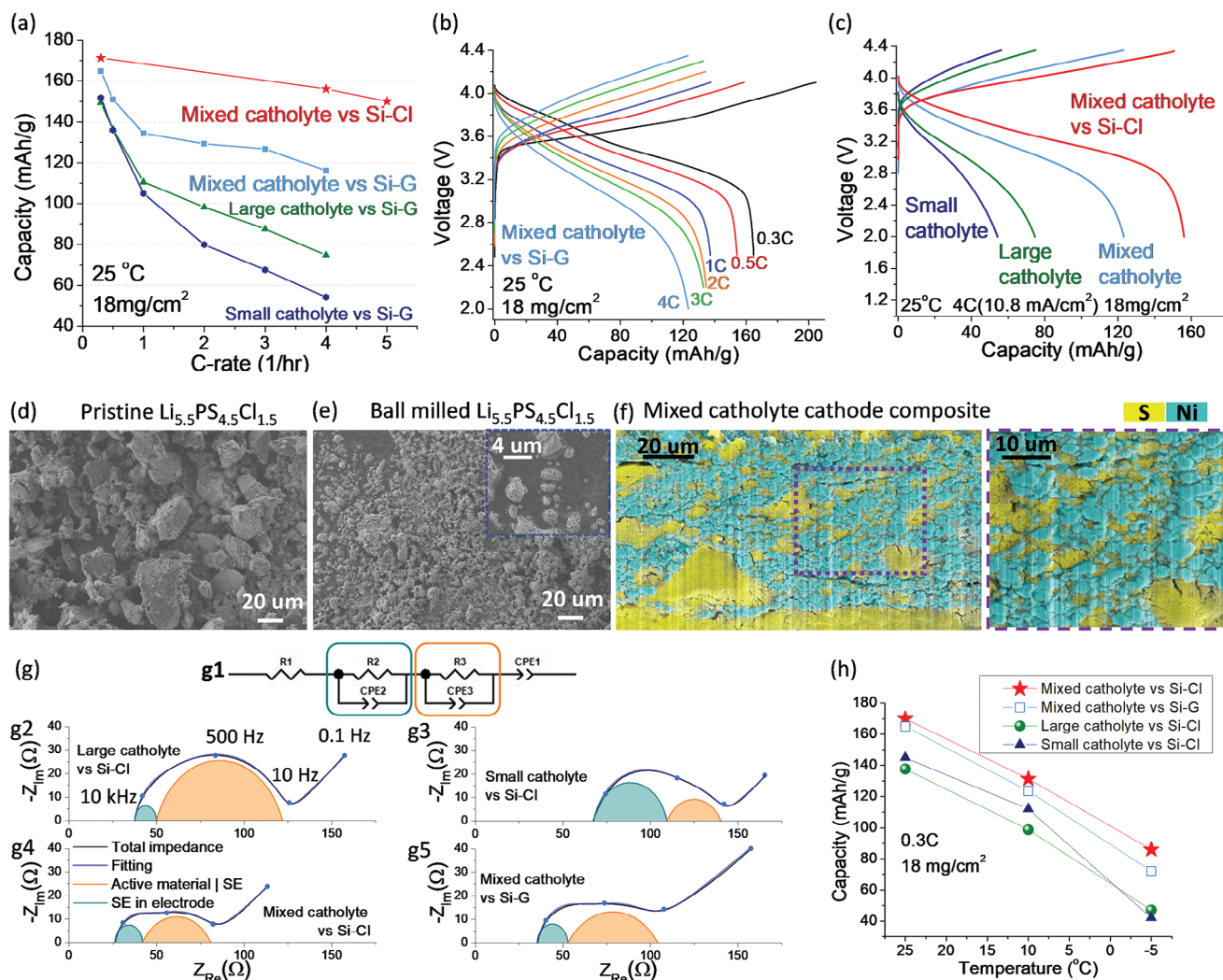
Figure 2. Electrode design for fast battery kinetics. a) Rate performance comparison for SSBs with different cell configuration at RT and a cathode loading of 18 mg cm^{-2}. The label of Si–G represents anode layers made by an Si–Graphite composite layer above a Li metal layer (i.e., Si–G|Li); while, Si–Cl represents the anode structure of a layer of Si and argyrodite Li$_{7-y}$PS$_{6-y}$Cl$_y$ (LPSCly) composite above a separate graphite layer and a separate Li metal layer in the battery assembly (i.e., Si–Cl|G|Li). The mixed catholyte represents mixed small and large particle size of argyrodite Li$_{5.5}$PS$_{4.5}$Cl$_{1.5}$ (LPSCl1.5) electrolyte in the cathode composite layer; while, small or large catholyte represents cathode layer with only small or only large LPSCl1.5 electrolyte particles. b) Corresponding charge–discharge voltage curves at different C-rates of the full cell configuration with mixed catholyte cathode versus Si–G anode (blue in [a]). c) Comparison of charge–discharge voltage curves at 4 C-rate of the full cells with different cell configuration. d,e) SEM of the pristine (large particle) LPSCl1.5 (d) and the ball milled (small particle) LPSCl1.5 particles (e). The inset in (e) is at a larger magnification. f) FIB-SEM-EDS mapping of the cross-section of mixed catholyte cathode composite. The inset on the right enlarges the region in the dashed rectangle on the left. g) Impedance spectra analysis and comparison for different cell configurations. h) Comparisons of capacities at various temperatures for different cell configurations.

layers of silicon–graphite composite layer above the Li metal layer (Si–G|Li) as the anode to pair with different cathode layer configurations. The cathode composite with mixed particle sizes of argyrodite electrolyte Li$_{5.5}$PS$_{4.5}$Cl$_{1.5}$ (LPSCl1.5) delivers much higher capacity from single crystal LiNi$_{0.83}$Mn$_{0.06}$Co$_{0.11}$O$_2$ (NMC) at high C-rates (light blue curve in Figure 2a) than the control cells with either large (green curve in Figure 2a) or small (dark blue in Figure 2a) electrolyte particles in the cathode layer. Figure 2b shows the corresponding voltage curves of the cell with optimized cathode at different C-rates, where cut-off voltages are adjusted at each C-rate for all batteries to compen-

sate for polarization at large current. Figure 2c shows the comparison of voltage curves for different cell configurations at 4 C-rate.

Figure 2d,e shows the SEM images of the as-synthesized pristine LPSCl1.5 with a particle size ≈20 um, and the ball milled LPSCl1.5 with a much-reduced particle size of ≈300 nm to 4 um. Figure 2f shows the cross-section focused ion beam scanning electron microscopy energy dispersive spectroscopy (FIB-SEM-EDS) of the mixed catholyte cathode composite. The existence of small LPSCl particles makes NMC particles well surrounded by solid electrolytes; while, the large particles of LPSCl provide fast

ADVANCED
SCIENCE NEWS

www.advancedsciencenews.com

ADVANCED
MATERIALS

www.advmat.de

Li ion conduction through them with the lowest possible local tortuosity.

On the anode side, to improve Li conductivity in the anode layer, we mix 20 wt% pristine $Li_{7-y}PS_{6-y}Cl_y$ (LPSCly) with pure silicon to form the Si–LPSCly (Si–Cl) composite layer and move the graphite to a thin separate layer between Li metal and Si–Cl layers to prevent the chemical reaction between Li and LPSCly (Si–Cl|G|Li). This design further improves the high rate performance (red curves in Figure 2a,c).

2.2. Kinetics Design for Nano Interfaces and Micron Thickness

To understand the cathode composite kinetics, we measure the impedance at 25 °C (Figure 2g) and at various temperatures (Figure S1, Supporting Information). In the circuit model to simulate the impedance spectra (Figure 2g1), R1 (interception at x axis) is used to represent the resistance of the connected electrolyte network including separator layers, catholyte, and anolyte, and a constant phase element (CPE1) is used to represent the Li diffusion in NMC. Two depressed semicircles are fitted at ≈500 Hz (R3-CPE3) and 10 kHz (R2-CPE2), respectively. The fitted results of R2 and R3 are presented in Table S1, Supporting Information.

The high-frequency 10 kHz semicircle is contributed by the Li ion transport through solid electrolyte within the electrode composite layers; while, the low-frequency 500 Hz semicircle is contributed by the interface between electrode active material and solid electrolyte in the composite matrices[20–22] at nano to submicron scale. This is supported by the analysis of Figure 2g. When only using large catholyte particles, we find small R2 (10 kHz) and large R3 (500 Hz). Conversely, when only using small catholyte particles, it shows the opposite trend of large R2 and small R3 (Figure 2g2,g3). The large electrolyte particle gives fast Li ion conduction with low local tortuosity at the expense of insufficient interface contact to cathode particle (Figure 1c left panel). In contrast, the small electrolyte particle gives slow Li ion conduction due to high tortuosity in the composite layer, but it can form good interface contact with cathode particle (Figure 1c middle panel). We thus conclude that R2 is decided by the Li ion conduction in the catholyte network; while, R3 is decided by the cathode–electrolyte interface contact. Therefore, when mixing large and small LPSCl1.5 in the cathode (Figure 1c right panel), both 10 kHz (R2-CPE2) and 500 Hz (R3-CPE3) semicircles become small, giving the lowest overall cathode resistance (Figure 2g4,g5) for an optimized ion conductivity in the cathode composite layer.

The activation energies (E_a) of interfaces are calculated and presented in Figure S1 and Table S1, Supporting Information. Interestingly, despite the smallest resistance from impedance measurement, the cell configuration of mixed catholyte cathode paired with Si–Cl anode gives an E_a of 284 meV, which is 37 meV higher than the large catholyte-only configuration and 86 meV higher than the small catholyte-only configuration. This is because E_a here corresponds to resistivity ρ rather than to resistance R, where $\sigma = \frac{1}{\rho} \propto \exp(\frac{-E_a}{kT})$.

The much smaller interface resistance R3 but higher resistivity (ρ) for the mixed catholyte cell than the large catholyte-only cell thus suggests that although adding small LPSCl1.5 particles

increases the resistivity at various interfaces, the overall interface contact area (A) is dramatically increased; thus, giving a much lower resistance ($R = \rho l/A$) in the cathode layer, where l is the interface thickness. Comparing the mixed catholyte cell with the small catholyte-only cell, the interface R3 is comparable because both cells now contain the small LPSCl1.5 particles. However, the much smaller resistance R2 but higher interface resistivity here in the mixed catholyte cell suggest that the existence of large catholyte particles with high bulk conductivity effectively transports Li ions across the thick catholyte network, which dramatically reduces R2.

Further, when comparing the anode configurations of Si–G|Li with Si–Cl|G|Li for the activation energy using the same mixed catholyte configuration, the latter is 42 meV larger than the former (Figure S1, Supporting Information), suggesting that adding electrolyte to the anode layer may introduce extra interface reaction to increase the E_a and interface resistivity, but the benefit of the LPSCl1.0 region with much higher bulk ionic conductivity than Si, Li–Si alloy, and graphite effectively reduces the R3 in the latter to 39 Ω (Figure 2g4) from the 51 Ω of the former case (Figure 2g5).

Figure 2h compares the specific capacities of different full cell configurations at 0.3 C-rate from RT to low temperatures. With the same mixed catholyte configuration, Si–Cl|G|Li anode shows better low temperature performance than the Si–G|Li anode; while, with the same Si–Cl|G|Li anode, the mixed catholyte configuration is much better than the other two configurations without mixing catholyte particle sizes.

We then cycled the full cell at RT using the best cell design with mixed catholyte cathode layer paired with Si–Cl|G|Li anode (**Figure 3a**). Three batteries with different cathode loading from 18 to 27 mg cm^{-2} could stably cycle with 2.5 to 4.6 mAh cm^{-2} at charge rate ranging from 5 to 3 C for more than 2400 to 4200 cycles. These batteries were cycled in an oscillating temperature range at RT from 22° to 30 °C without temperature control; thus, a fluctuating capacity in a range for each battery, suggesting the robustness of our design against temperature fluctuations near RT. Figure 3b–d shows the corresponding voltage profiles with smooth curves throughout the cycling, which further confirm a slow capacity decay without any short circuit. At even higher loading, for example, ≈7 and ≈10 mAh cm^{-2}, the battery could still cycle at 1 and 0.5 C (Figure 1; Figure S2, Supporting Information). Figure 3e–g shows the corresponding specific capacity of NMC in the three batteries starting at ≈150 mAh g^{-1} and coulombic efficiency slightly fluctuating around 100% due to temperature fluctuation, consistent with the very slow speed of capacity decay. Such high power density at high areal capacity for the long cycling of SSBs is for the first time demonstrated through the fast kinetics design at the battery device level (Figure 1).

We do not add carbon additives because at the NMC:catholyte weight ratio of 7:3, electronic conductivity of the percolated NMC network is high enough.[11] As seen in Figure S3a, Supporting Information, at low NMC:LPSCl1.5 weight ratio of 2:8 or NMC:LGPS weight ratio of 4:6, the NMC network loses electronic percolation; thus, giving nearly zero capacity. Adding carbon nano fiber (CNF) can build electronic percolation in the cathode layer; and thus, dramatically increase the capacity. In contrast, at high NMC:catholyte weight ratio of 7:3, adding CNF
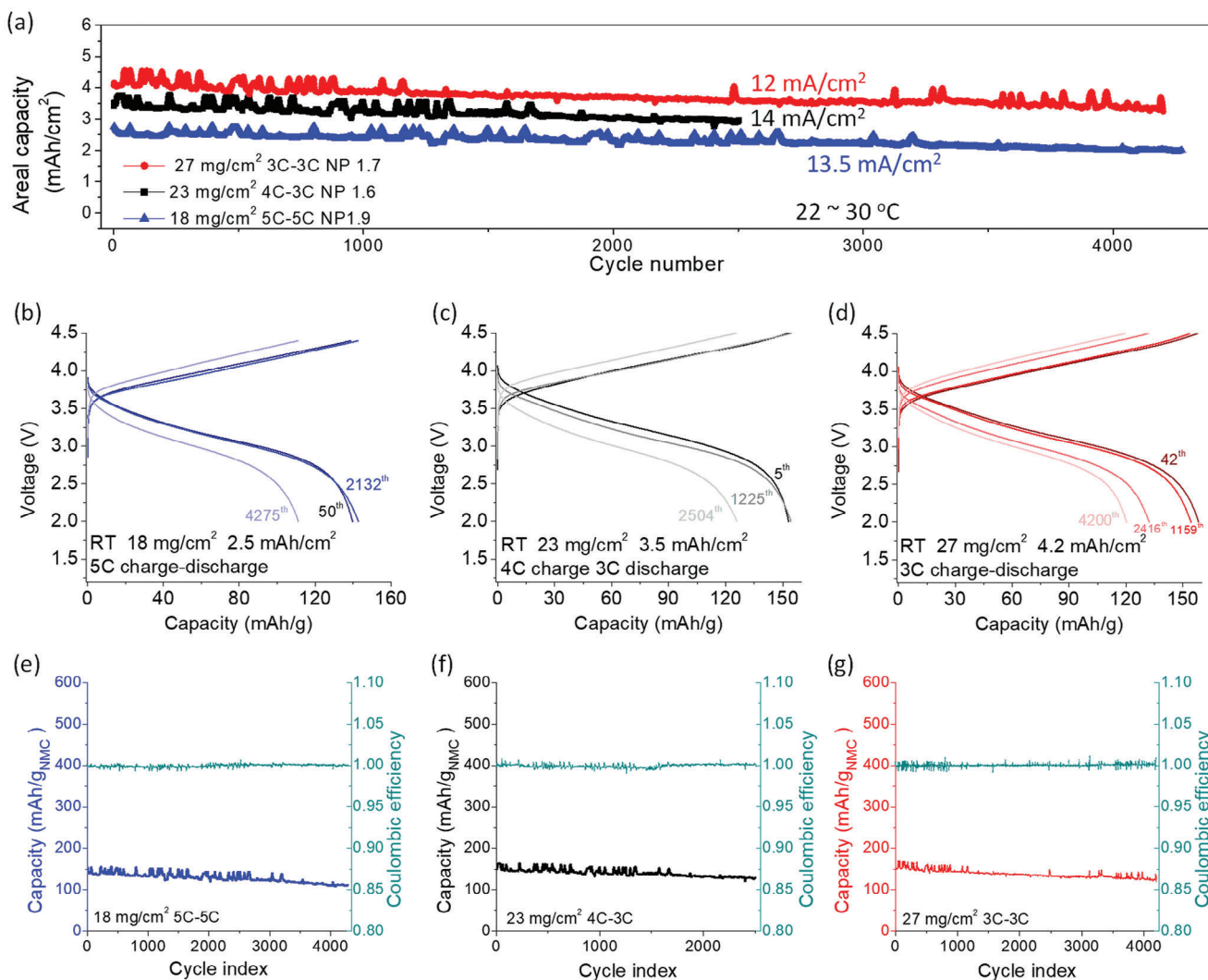
**ADVANCED
SCIENCE NEWS**

www.advancedsciencenews.com

**ADVANCED
MATERIALS**

www.advmat.de

Figure 3. a) Cycling performance of full cells with the mixed catholyte paired with Si–Cl anode configuration at RT (temperature fluctuates in a range of 22–30 °C without environmental temperature control), with different areal capacity (≈2.5–4.6 mAh cm⁻² or ≈18–27 mg cm⁻² cathode loading), C-rate (≈3–5 C-rate or ≈12–14 mA cm⁻² current density), and nominal NP ratio (≈1.7–1.9), at a specific capacity ≈150 mAh g_{NMC}^{-1}. The central electrolyte separator layer used our iodine doped LPSCl1.5-I (See the Experimental Section). b) Cycling performance in pouch cell at 10 MPa external pressure and 5 C charge and discharge with a separator thickness of 75 um. b–d) Corresponding voltage curves to (a) as labeled in each panel. e–g) Corresponding specific capacity of NMC and coulombic efficiency to the three batteries in (a) as labeled in each panel. Note that the lowest capacities in initial cycles, corresponding to the lowest temperature in the fluctuating range, were used to plot Figure 1a.

slightly decreases the capacity of mixed-catholyte composite and large-catholyte composite and gives marginal benefit to the small-catholyte composite with the highest tortuosity among the three types of cathode composites. This suggests that all three cathode composite configurations with 70 wt% of NMC are already electronically percolated; while, CNF and/or CNF-induced decomposition will only increase the ionic tortuosity.

2.3. Anode Kinetics Design Breaking the Limit from Rate–Voltage Correlation

We now try to understand the significant kinetic improvement of the Si–Cl|G|Li anode over the Si–G|Li anode. We first compare

the charge–discharge voltage curve of the second cycle at a slow rate of 0.5 C for SSBs made by mixed catholyte cathode paired with Si–G|Li anode of different Si weight percent (**Figure 4a,b**). Li metal anode liquid electrolyte battery is used as the reference for 0% Si. During charge, the initial voltage drops from 0% Si to 20% Si, and then, the voltage profiles seem to converge from 35% Si up to 100% Si without further voltage drop (Figure 4a). In addition, note that the initial voltage at the turning point in the charge voltage profile (See the Experimental Section; Figure S4, Supporting Information) is kept in a narrow voltage range of 0.1 V from 3.6 to 3.5 V for batteries with 20–100% Si. This process is saturated due to the relatively flat voltage profile of Si–G anode when Li is charged toward it (Figure S5, Supporting Information).
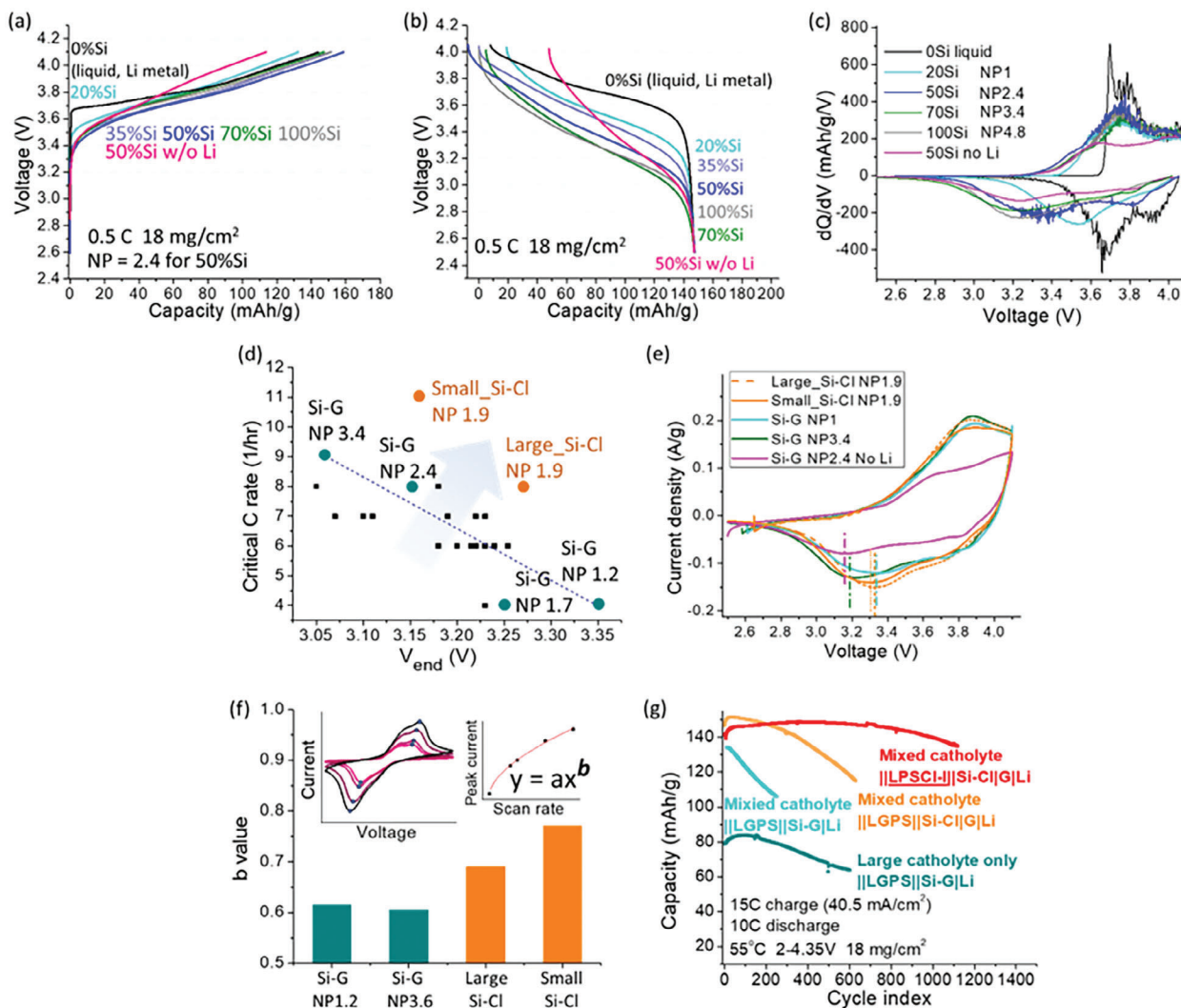
Figure 4. Electrochemistry analysis and comparison of anode configurations. a) Charge and b) discharge voltage curves of SSB with Si–G|Li anode of the same total weight of Si and graphite but different Si wt% and c) corresponding dQ/dV curves. d) The tradeoff relationship between critical C rate at short circuit and the turning point voltage at the end of discharge at 0.3 C for SSBs with different anode configuration. The turning point is defined as the voltage at the capacity of full discharge capacity minus 15 mAh g^{-1}. Anode configuration includes Si–G|Li (green dots) and doped Si–G|Li (black dots) anode at different NP ratios and the Si–Cl|G|Li anodes with small or large Si and LPSCly particles (orange dots). e) Comparison of CV curves of full cells with different anodes. f) The *b* value obtained from CV cycling test of cells with different anode_1|electrolyte|anode_2 configurations. g) Cycling performance comparison for different cathodes (mixed catholyte vs large catholyte only), anode (Si–G|Li vs Si-Cl|G|Li), and central separator (LGPS vs LPSCl-I) layer combinations at extreme C-rate of 15 C charge (40.5 mA cm^{-2}) and 10 C discharge.

During discharge, the voltage profiles are much more separated with the Si composition change in the Si-graphite composite layer, with higher average discharge voltage for lower Si percentage (Figure 4b). Especially, the end-of-discharge voltage at the turning point distributes in a wide voltage range of 0.4 V from 3.3 to 2.9 V for batteries with 20–100% Si. This charge–discharge asymmetry can also be observed in the dQ/dV analysis of these voltage profiles (Figure 4c), where the peaks in discharge show a shift in a much broader voltage range than the charge ones. For the control battery of liquid electrolyte cell with pure Li metal as the anode (black curve in Figure 4c), the discharge dQ/dV peak is at 3.7 V, and the most capacity is above 3.5 V. For the other control battery of Si–G anode solid-state cell without Li metal foil to provide any pre-lithiation to Si (pink curve in Figure 4c), the

discharge dQ/dV peak is the lowest among all the batteries at 3.23 V, suggesting that the anode exhibits the highest portion of Si (de)lithiation capacity. Batteries with Si–G|Li anodes show CV peak voltages between 3.23 and 3.7 V, where lower NP ratio (calculated based on nominal capacity of Si anode) is correlated with higher discharge voltage. This suggests that pre-lithiated Si–G anode by the Li metal foil in Si–G|Li in comparison with the non-prelithiated one exhibits a higher portion of lithium plating and stripping capacity and lower portion of Si lithiation and delithiation capacity.

We further measure the critical C-rate before short circuit for SSBs with thick cathode of 18 mg cm^{-2} loading paired with different anode. These batteries show 150 mAh g^{-1} specific capacity (2.7 mAh cm^{-2} areal capacity) in the charge regardless of the

**ADVANCED
SCIENCE NEWS**

www.advancedsciencenews.com

**ADVANCED
MATERIALS**

www.advmat.de

voltage cut-off. In the test, we increase the C-rate in every cycle from 0.3 C up to the C-rate with clear signal of short circuit (Figure S4, Supporting Information). We define the first C-rate in the series when short circuit happens as the critical C-rate. A new correlation is unveiled, where critical C-rate negatively correlates with the end-of-discharge voltage turning point at 0.3 C-rate (V_{end}) for all the batteries we evaluate (Figure 4d). These batteries include anode configurations of Si–G|Li at different nominal NP ratio and doped Si–G|Li at a fixed NP ratio with small amount of additive (Ge, Sn, Ag, etc.; see Table S3, Supporting Information for more details) mixed to the Si powder by ball mill as well. The anticorrelation in Figure 4d here suggests that higher discharge voltage of the cell, and hence, more lithium metal capacity and less Si capacity at anode, is associated with lower critical C-rate; and hence, easier to short. This makes sense as a higher portion of Li metal plating and stripping at anode makes the anode behave more like Li metal anode, which must suffer from the issue of dendrite growth more easily at high current densities.

For SSB application, it will thus be of a particular importance to seek solutions to break such a correlation, so that, batteries can exhibit both high critical C-rate for high power density and higher discharge voltage for increased energy density, that is, moving toward the right upper corner in Figure 4d is preferred. This is to say, we want an anode design that can keep a significant portion of Li metal plating and stripping, but, without the dendrite issue at high current density. We find that the Si–Cl|G|Li anode configuration successfully breaks the correlation in such a way. When small particles of 1 um Si and 3 um LPSCl1.0 are mixed at 80:20 weight ratio (Small_Si-Cl), the battery shows a high critical C-rate above 10 C and a turning point voltage of 3.15 V, and when large particles of 20 um Si and 20 um LPSCl1.5 (Large_Si-Cl) are mixed, the battery shows a higher turning point voltage at 3.27 V and a critical C-rate at 8 C.

Like the dQ/dV analysis in Figure 4c, we compare the CV curves of Si–Cl|G|Li anodes with those of Si–G|Li anodes (Figure 4e). The three anodes are at different NP ratios and prelithiation levels. The anode of Si–G|Li at NP = 1.0, with Li metal layer for pre-lithiation and low NP to limit the lithiation capacity and promote the plating one, should be at the high-voltage end of the anticorrelation in Figure 4d. In contrast, the anode of Si–G at NP = 2.4 is without Li metal in the battery assembly, and hence, no pre-lithiation to Si, and that of Si–G|Li at NP = 3.4 has sufficient Si for more lithiation and less Li plating, both of which thus should be at the low-voltage end. We find that the discharge CV peak positions of the two Si–Cl|G|Li anodes with NP ratio of 1.9 are very close to the Si–G|Li anode with NP ratio of 1. This suggests that mixing LPSCl1.5 electrolyte particles with Si particles for Si–Cl|G|Li can significantly reduce the (de)lithiation capacity per Si particle and increase the capacity portion of Li metal stripping and plating.

The advantage of the Si–Cl|G|Li anode is that it still maintains a much higher critical C-rate against Li dendrite penetration than those Si–G|Li anodes at higher NP values. As shown in Figure 4d, the critical C-rate of Si–Cl|G|Li anode at NP = 1.9 is close to that of the Si–G|Li anode at NP = 2.4 or above, and at the same NP ratio, the former anode design gives much higher critical C-rates. Therefore, the capacity portion of Li metal plating/stripping in Si–Cl|G|Li must happen at distinct locations in the anode region

from that of the Si–G|Li anode, so that, the Li dendrite growth is much less preferred. As the soft sulfide electrolyte can also reduce the porosity of the Si layer in the Si–Cl mixture and help transport Li$^+$ through the Si–Cl layer, more Li metal will plate at the bottom region near the G-Li layer, and less Li deposition will happen in the region close to the interface with the electrolyte separator layer in Si–Cl|G|Li (Figure 1d right panel). In contrast, in the Si–G|Li anode, Li will plate in the pore region of the Si–G layer and higher C-rate will tend to force more Li metal to plate near the interface to the electrolyte separator layer due to kinetic limits, where Li dendrite can grow more easily to cause short circuit penetration (Figure 1d left panel). Moreover, Cl1.5 and Cl1.0 as the solid electrolyte have ≈four orders of magnitude larger Li diffusivity than graphite and Li–Si alloy;[23–25] so that, they can extract Li from the anode more efficiently with lower kinetic barrier to reach a higher discharge voltage. Specifically, the Si–Cl|G|Li anode can be even thinner than the Si–G|Li anode (Figure S6, Supporting Information) as the graphite layer in the former design is very thin. Thus, in the large_Si-Cl configuration, the 20 um LPSCl1.5 particle in the Si layer can directly connect the neighboring layers of the G|Li and the electrolyte separator to extract Li more efficiently than the small_Si-Cl configuration, giving a higher V_{end}.

To understand more about the kinetics mechanism behind the phenomenon, we perform cyclic voltammetry (CV) measurement (Figure S7, Supporting Information) of different anode_1| electrolyte |anode_2 cells at a set of sweeping rates to extract the b value that characterizes the overall kinetics[26] of the anode configuration, where the anode contains Si–G with different NP ratios and Si–Cl with different particle sizes. In general, the b-value ranges from 0.5, where the process is diffusion limited, to 1.0, where a surface limiting process dominates. Figure 4f shows that the b-value is much higher for Si–Cl|G|Li anodes, suggesting better overall kinetics, consistent with their higher critical C-rate.

Our fast kinetics design of SSB at both cathode and anode layers also leads to an extreme C-rate capability of 15 C charge (40.5 mA cm^{-2}) and 10 C discharge at 55 °C that can be cycled for 1100 cycles at ≈150 mAh g^{-1} (Figure 4g). The voltage curves keep a smooth shape throughout the battery cycling, indicating no short circuit even if the battery is cycled at such an extreme current density for more than 1000 cycles (Figure S2e, Supporting Information). Note that here the central electrolyte layer in the multi-separator-layer design[2] uses iodine doped argyrodite of Li$_{5.5}$PS$_{4.5}$Cl$_{1.35}$I$_{0.15}$ (LPSCl-I) with optimized dynamic voltage stability for Li dendrite constriction.[3] Without such an electrolyte design, an NMC-Cl1.5(7:3)|Cl1.5|LGPS|Cl1.5|Si-G|Li full cell based on LGPS central electrolyte layer shows a low initial specific capacity of 80 mAh g^{-1} that drops to 80% after only 600 cycles. With cathode optimization only, the capacity increases to 135 mAh g^{-1}, but the cycle life decreases to 250 cycles. With additional Si–Cl|G|Li anode, both capacity and cycle life can be increased dramatically.

3. Conclusion

In summary, a leap in full cell kinetics at high cathode loading and area capacity has been achieved by designing hierarchical structures in electrode composites. In the cathode, we use

**ADVANCED
SCIENCE NEWS**

www.advancedsciencenews.com

**ADVANCED
MATERIALS**

www.advmat.de

the large electrolyte particle as a highway for Li-ion conduction through the thick cathode layer plus the small electrolyte particle to ensure the nano to submicron scale interface contact between NMC particle and the catholyte matrix. In the anode, adding solid electrolyte to the Si layer significantly improves the overall anode kinetics, which increases the critical C-rate and discharge voltage. The design principles unveiled by our work here will help understand critical kinetic processes in the battery device that limit the fast cycling at high cathode loading and speed up the design of high performance SSBs.

4. Experimental Section

Materials Synthesis: Li5.5PS4.5Cl1.5 (LPSCl1.5) and $Li_{5.5}PS_{4.5}Cl_{1.35}I_{0.15}$ (LPSCl-I) were prepared by high energy ball milling and a subsequent annealing process. Stoichiometric amounts of Li2S (99.9% purity, Alfa Aesar), P2S5 (99% purity, Sigma–Aldrich), LiCl (99% purity, Alfa Aesar), and LiI (99% purity, Sigma–Aldrich) were milled for 16 h in a planetary mill PM200 (Retsch GmbH, Germany) under a protective argon atmosphere, followed by sintering at 550 °C in a quartz tube.

Full Cell Assembly: A Li foil with a thickness of 15 µm was covered by a silicon–graphite composite film made by mixing silicon, graphite (BTR, China), and PTFE with a weight ratio of 47.6%:47.6%:4.8% (Si–G|Li), or, by stacking graphite film and Si–$Li_{7-y}PS_{6-y}Cl_y$ (LPSCly) composite film (Si–Cl|G|Li), where Si: LPSCly: PTFE = 76.2 wt%: 19 wt%: 4.8 wt% in the Si–Cl layer. Si–Cl thickness labeled in Figure 1b was estimated by the Si–G thickness measured in the SEM in Figure S6, Supporting Information, NP ratios and materials densities. Nominal NP ratio was calculated based on the theoretical capacity of Si (practically 3000 mAh g^{-1}) and NMC83 (200 mAh g^{-1}). All cathode loading was at 18 mg cm^{-2} unless otherwise labelled in the plot. In Figures 2a–c,g,h and 4g, cells have a NP ratio of 2.4 for all the Si–G cells and NP 1.9 for the Si–Cl cell. In Figure 4a,b,c, the Si to graphite weight ratio is changed in cells with a changing NP ratio as labelled in Figure 4c at a fixed cathode loading of 18 mg cm^{-2}. In Figure 4d, all the doped Si–G|Li anode cells are at NP 2.4, and all cells are at 18 mg cm^{-2} NMC. The battery with Si–Cl|G|Li anode and 18 mg cm^{-2} cathode loading in Figures 2a,c and 3a is the same battery with the LPSCl1.5 mixed with Si in anode. All other Si–Cl|G|Li batteries were with LPSCl1.0 (Pascal, 3 um) mixed in the Si–Cl layer in the anode. LPSCl to Si weight ratio was 2:8 in the Si–Cl layer. The cathode dry film was made by mixing 30 wt% solid electrolyte, 70 wt% single-crystal LiNi0.83Mn0.1Co0.07O2 (NMC83, 1–5-µm particle size, MSE Supplies), and an additional 3 wt% PTFE. For large-only catholyte configuration, all the 30 wt% solid electrolyte was the as-synthesized LPSCl1.5. For small-only catholyte configuration, all 30 wt% solid electrolyte was ball-milled LPSCl1.5. The ball milling was conducted using MM500 nano (Retsch) with 8 Hz for 8 h. For mixed catholyte, 20 wt% small LPSCl1.5 and 10 wt% large LPSCl1.5 were used. All batteries used multi-electrolyte-layer separator between cathode and anode layers, with 20 mg LPSCl1.5 and 100 mg LPSCl-I as LPSCl1.5|LPSCl-I|LPSCl1.5 separator configuration. The full battery, with a structure of anode|LPSCl1.5|LPSCl-I|LPSCl1.5|cathode, was pressed together in a homemade pressurized cell at 400 MPa and kept at 50 MPa during testing. All batteries were assembled in an argon atmosphere glovebox. For RT battery cycling test, the temperature was not controlled to be constant and was fluctuating between 22 °C and 30 °C through the cycling test measured by thermometer. For non-cycling tests, the batteries were evaluated inside a Memmert hpp110 or Espec environmental chamber with temperature control. Battery cycling test was conducted using an Arbin instrument.

Electrochemical Impedance Spectra (EIS): The EIS of full cells were measured in a Solartron 1455A, over the frequency range from 0.1 Hz to 1 MHz, with an AC measuring voltage of 0.01 V, after testing the 0.3 C capacity between 2.5 and 4.1 V at RT, 10 °C, and −5 °C, respectively. All Nyquist plots were fitted with R(RQ)(RQ)Q equivalent circuit by ZView.

Cyclic Voltammetry (CV): CV of anode_1| separator |anode_2 cells with Li metal layers on both sides was conducted at Solartron 1470E between −1.5 and 1.5 V, with different sweep rates from 0.5 to 3 mV s^{-1}. The 0.5 mV s^{-1} cycle was used as an activation cycle. Peak currents at each scan rate were plotted versus scan rate and fitted with $y = ax^b$ to extract the exponent b value. Anode_1 was always the configuration of Si + 20 wt%_Cl1.5|G|Li using large particles of Si and LPSCl1.5 (Large Si-Cl). Anode_2 was different for four different cell configurations of Si–G|Li at NP1.2, Si-G|Li at NP3.6, Large_Si-Cl|G|Li, and Small_Si-Cl|G|Li using small particles of Si and LPSCl1.5, respectively. NP1.2 or NP 3.6 was calculated based on a hypothetical full cell as if the anode was paired with an 18 mg cm^{-2} NMC cathode. Similarly, the two Si–Cl cells were at NP 1.9. More details can be found in Figure S7, Supporting Information.

SEM: FEI Helios 660 was used for the cross-section focused ion beam scanning electron microscopy energy dispersive spectroscopy (FIB-SEM-EDS) imaging. The cycled pellet was transferred from an argon-filled glovebox using a sealed plastic bag. The sample was exposed to air within 1 min during transfer. Ga$^+$ milling procedures were conducted to create a cleaned cross-section region at different currents. SEM-EDX imaging was conducted using the inner EDAX tools and detector of the instrument.

Supporting Information

Supporting Information is available from the Wiley Online Library or from the author.

Conflict of Interest

Y.W. and X.L. reported a US provisional patent application.

Author Contributions

Y.W. and X.L. conceived the fast kinetics design. X.L. supervised all aspects of the research. Y.W. performed the experiments. Y.W. and X.L. analyzed the results and wrote the manuscript.

Data Availability Statement

The data that support the findings of this study are available from the corresponding author upon reasonable request.

[1] Y. Li, S. Song, H. Kim, K. Nomoto, H. Kim, X. Sun, S. Hori, K. Suzuki, N. Matsui, M. Hirayama, T. Mizoguchi, T. Saito, T. Kamiyama, R. Kanno, *Science* **2023**, *381*, 50.

[2] L. Ye, X. Li, *Nature* **2021**, *593*, 218.

[3] Y. Wang, L. Ye, X. Chen, X. Li, *JACS Au* **2022**, *2*, 886.

[4] E. Gil-González, L. Ye, Y. Wang, Z. Shadike, Z. Xu, E. Hu, X. Li, *Energy Storage Mater.* **2022**, *45*, 484.

[5] E. A. Wu, C. Jo, D. H. Tan, M. Zhang, J.-M. Doux, Y.-T. Chen, G. Deysher, Y. S. Meng, *J. Electrochem. Soc.* **2020**, *167*, 130516.

[6] W. Yan, Z. Mu, Z. Wang, Y. Huang, D. Wu, P. Lu, J. Lu, J. Xu, Y. Wu, T. Ma, M. Yang, X. Zhu, Y. Xia, S. Shi, L. Chen, H. Li, F. Wu, *Nat. Energy*, **8**, 800.

[7] Y. Kato, S. Hori, T. Saito, K. Suzuki, M. Hirayama, A. Mitsui, M. Yonemura, H. Iba, R. Kanno, *Nat. Energy* **2016**, *1*, 16030.

[8] D. H. S. Tan, Y.-T. Chen, H. Yang, W. Bao, B. Sreenarayanan, J.-M. Doux, W. Li, B. Lu, S.-Y. Ham, B. Sayahpour, J. Scharf, E. A. Wu, G. Deysher, H. E. Han, H. J. Hah, H. Jeong, J. B. Lee, Z. Chen, Y. S. Meng, *Science* **2021**, *373*, 1494.

[9] D. Cao, X. Sun, Y. Li, A. Anderson, W. Lu, H. Zhu, *Adv. Mater.* **2022**, *34*, 2200401.

[10] T. Shi, Q. Tu, Y. Tian, Y. Xiao, L. J. Miara, O. Kononova, G. Ceder, *Adv. Energy Mater.* **2020**, *10*, 1902881.

[11] P. Minnmann, L. Quillman, S. Burkhardt, F. H. Richter, J. Janek, *J. Electrochem. Soc.* **2021**, *168*, 040537.

[12] H. Shen, E. Yi, M. Amores, L. Cheng, N. Tamura, D. Y. Parkinson, G. Chen, K. Chen, M. Doeff, *J. Mater. Chem. A* **2019**, *7*, 20861.

[13] D. W. McOwen, S. Xu, Y. Gong, Y. Wen, G. L. Godbey, J. E. Gritton, T. R. Hamann, J. Dai, G. T. Hitz, L. Hu, E. D. Wachsman, *Adv. Mater.* **2018**, *30*, 1707132.

[14] Y.-G. Lee, S. Fujiki, C. Jung, N. Suzuki, N. Yashiro, R. Omoda, D.-S. Ko, T. Shiratsuchi, T. Sugimoto, S. Ryu, J. H. Ku, T. Watanabe, Y. Park, Y. Aihara, D. Im, I. T. Han, *Nat. Energy* **2020**, *5*, 299.

[15] S. Poetke, F. Hippauf, A. Baasner, S. Dörfler, H. Althues, S. Kaskel, *Batteries Supercaps* **2021**, *4*, 1323.

[16] S. Cangaz, F. Hippauf, F. S. Reuter, S. Doerfler, T. Abendroth, H. Althues, S. Kaskel, *Adv. Energy Mater.* **2020**, *10*, 2001320.

[17] S. Luo, Z. Wang, X. Li, X. Liu, H. Wang, W. Ma, L. Zhang, L. Zhu, X. Zhang, *Nat. Commun.* **2021**, *12*, 6968.

[18] Z. Zhang, L. Wu, D. Zhou, W. Weng, X. Yao, *Nano Lett.* **2021**, *21*, 5233.

[19] M. A. Kraft, S. Ohno, T. Zinkevich, R. Koerver, S. P. Culver, T. Fuchs, A. Senyshyn, S. Indris, B. J. Morgan, W. G. Zeier, *J. Am. Chem. Soc.* **2018**, *140*, 16330.

[20] T.-T. Zuo, R. Rueß, R. Pan, F. Walther, M. Rohnke, S. Hori, R. Kanno, D. Schröder, J. Janek, *Nat. Commun.* **2021**, *12*, 6669.

[21] J. S. Lee, Y. J. Park, *ACS Appl. Mater. Interfaces* **2021**, *13*, 38333.

[22] W. Zhang, D. A. Weber, H. Weigand, T. Arlt, I. Manke, D. Schröder, R. Koerver, T. Leichtweiss, P. Hartmann, W. G. Zeier, J. Janek, *ACS Appl. Mater. Interfaces* **2017**, *9*, 17835.

[23] J. Li, N. J. Dudney, X. Xiao, Y. T. Cheng, C. Liang, M. W. Verbrugge, *Adv. Energy Mater.* **2015**, *5*, 1401627.

[24] J. H. Park, H. Yoon, Y. Cho, C.-Y. Yoo, *Materials* **2021**, *14*, 4683.

[25] P. Adeli, J. D. Bazak, K. H. Park, I. Kochetkov, A. Huq, G. R. Goward, L. F. Nazar, *Angew. Chem., Int. Ed.* **2019**, *58*, 8681.

[26] C.-H. Lai, D. S. Ashby, T. C. Lin, J. Lau, A. Dawson, S. H. Tolbert, B. S. Dunn, *Chem. Mater.* **2018**, *30*, 2589.